Optics Communications 537 (2023) 129451

Contents lists available at ScienceDirect

Optics Communications

journal homepage: www.elsevier.com/locate/optcom

Active compensation for perturbed coaxial reflecting space telescope using defocus point spread function and convolutional neural network

Bingdao Li [a], Xiaofang Zhang [a,*], Yun Gu [b], Shangnan Zhao [c], Jun Chang [a]

[a] School of Optics and Photonics, Beijing Institute of Technology, Beijing 100081, China
[b] Shanghai MicroPort MedBot (GROUP) Co., Ltd, Shanghai 200120, China
[c] Changchun Institute of Optics Fine Mechanics and Physics Chinese Academy of Sciences, Chinese Academy of Sciences, Changchun 130033, China

ARTICLE INFO

Keywords:
Active fast compensation
Misalignments
Figure errors
Convolutional neural network
Coaxial reflecting space telescope

ABSTRACT

Active compensation for perturbed coaxial reflecting space telescope (CRST) is an effective and important means to improve the image quality, which has been widely used in the field of astronomical observation. The existing compensation methods have disadvantages of complicated structure, high-cost and poor efficiency. Aiming to solve these problems, in this paper, a novel active compensation method for perturbed CRST based on defocus point spread function (PSF) and well-trained convolutional neural network (CNN) is proposed. First, the optimal compensation strategy for perturbed CRST by adjusting the secondary mirror (SM) is presented, and the nonlinear mapping between the defocus PSF at the field point of interest and five kinds of misalignments of SM is established by utilizing CNN. Then, two alignment schemes either using single-field or multi-field defocus PSFs to obtain the adjustments of SM are proposed, and the simulation proofs show that the image quality can be improved by using our method to implement the active compensation for perturbed CRST. Finally, the influences of image noise and high-order figure errors of primary mirror (PM) on the compensation effect are investigated respectively. Compared with the existing compensation methods, the proposed method requires neither a dedicated wavefront sensor nor driving active correction components repeatedly nor a lot of iterations to optimize a metric function, which is suitable for in-orbit active fast compensation for perturbed CRST.

1. Introduction

Space telescopes not only avoid the blurring effects caused by atmospheric turbulence, but also can achieve wide-band imaging. Among them, coaxial reflection space telescopes (CRSTs) have been widely used in space remote sensing after decades of development. The typical representatives such as Hubble Space Telescope launched into low-Earth orbit [1] and James Webb Space Telescope at second Lagrange point [2], play an important role in the field of astronomical observation.

When a CRST works in orbit, due to its own errors of design, manufacturing and alignment and the influences of external environment such as temperature change and gravity effect, the image quality of perturbed system will deteriorate caused by both the figure errors of primary mirror (PM) and the misalignments of secondary mirror (SM) or tertiary mirror (TM). To solve the problem, active optical methods [3–6] are usually utilized to improve the image quality of perturbed system. In active optics, it is ideal for the perturbed system to be restored to the nominal design state by arbitrarily adjusting each optical element to compensate for the misalignments and figure errors. However, in practice, the cost of restoring these perturbed components is huge and the system performance should be compensated for as easily as possible. The optimal strategy is to compensate for aberrations of the perturbed telescope by adjusting the smaller mirror such as the SM [7–9].

Two kinds of traditional methods have been used to realize the system aberration compensation. One kind of method including sensitivity table method (STM) [10], merit function regression (MFR) method [11], nodal aberration theory (NAT) method [12–14] and artificial neural network (ANN) method [15] requires employing a wavefront sensor such as the Shack–Hartmann wavefront sensor (SH) [16] or phase retrieval (PR) method [17,18] to sense the wavefront aberration and calculate the perturbations. Obviously, on the one hand, the use of wavefront sensors increases the complexity and cost of the system, and on the other hand, the PR method needs a beam splitter and an additional detector or translating the image plane or using weak lenses in a filter wheel to obtain a pair of intensity images with defocus diversity, resulting in the slight uncertainty of the system, besides, the PR method performs massive computations, which is time-consuming.

* Corresponding author.
E-mail addresses: 18844169395@163.com (B. Li), zhangxf@bit.edu.cn (X. Zhang), yunxia0371@163.com (Y. Gu), 18810575846@163.com (S. Zhao), optics_chang@126.com (J. Chang).

https://doi.org/10.1016/j.optcom.2023.129451
Received 16 January 2023; Received in revised form 19 March 2023; Accepted 19 March 2023
Available online 22 March 2023

Although increased computation time is not really an issue for space telescope, a fast alignment is attractive in practice.

The other kind of method does not need the wavefront sensing but uses a specific optimization algorithm to find the extreme value of the metric function established by the light intensity information on the detector, and the wavefront aberrations are compensated for when the metric function converges to its extreme value. In this type of method, the optimization algorithms are usually divided into two categories, one is model-free algorithm, such as simulated annealing algorithm [19], genetic algorithm [20] and stochastic parallel gradient descent algorithm [21], etc. These model-free methods are time-consuming and easy to fall into the local optimum due to the inaccuracy of metric function or control parameters. The other category is model-based algorithm [22,23], which can simplify the multiple iterative search to a deterministic direct solution, and the convergence speed of algorithm is greatly improved. Nevertheless, both model-based and model-free methods need to repeatedly drive the active correction elements to minimize the wavefront aberration, which reduces the stability of optical system and shortens the mechanical life of optical elements.

In recent years, the deep learning method based on the point spread function (PSF) has become an important way for in-orbit aberration compensation. Convolutional neural network (CNN) was used to establish the nonlinear relationship between PSF at the single field point and four misalignments of SM, and the prediction of the misalignments of SM of Ritchty–Chrétien optical system was preliminary realized assuming other errors do not exist [24]. For a CRST, all the optical elements might be perturbed in orbit, some methods should be developed to compensate for the misaligned or deformed optical elements simultaneously. Taking the coaxial three-mirror anastigmat (TMA) telescope as an example, this paper mainly focuses on how to use SM as the active component to compensation with misaligned SM, TM and deformed PM, and the proposed method is applicable to other CRSTs.

This paper is organized as follows. In Section 2, based on the principle that the misalignments and low-order figure errors of optical components can induce the same type of aberrations, the optimal compensation strategy for perturbed coaxial TMA telescope is proposed. Two alignment schemes either using single-field or multi-field defocus PSFs are proposed to calculate the adjustments of SM. In Section 3 and Section 4, a typical coaxial TMA telescope is taken as an example to verify our proposed method. Furthermore, the influences of image noise and high-order figure errors of PM on the compensation effect are investigated respectively. In addition, the proposed method is compared with STM in case of single-field alignment. In Section 5, the conclusions are given.

2. Method

Despite the variety of CRSTs, their basic system structures are same. In our study, the method, simulations and analyses are illustrated by taking the coaxial TMA telescope as an example and can be extrapolated to other CRSTs.

2.1. The optimal compensation strategy with SM

Based on NAT, for a coaxial TMA telescope having PM as the aperture stop and a real intermediate image plane between SM and TM, the misalignments of SM and TM and the low-order figure errors of PM can induce the same type of aberrations namely coma, astigmatism and defocus [25]. It is possible to compensate for the corresponding induced aberrations by adjusting other components with motion mechanisms. In our proposed method, the optimal compensation strategy for perturbed coaxial TMA telescope with misaligned SM and TM and deformed PM by adjusting SM is adopted, which can improve the image quality and meet the required system performance. This compensation process is performed as follows:

At the field point (x, y), the wavefront aberration of perturbed coaxial TMA telescope with misaligned SM and TM and deformed PM can be expressed as

$$\begin{aligned} W_{total}(x,y) &= W_H(x,y) + W_{PM}(x,y,a5,a6,a7,a8) \\ &+ W_{SM}(x,y,D_{SMx},D_{SMy},D_{SMz},T_{SMx},T_{SMy}) \\ &+ W_{TM}(x,y,D_{TMx},D_{TMy},D_{TMz},T_{TMx},T_{TMy}), \end{aligned} \tag{1}$$

where W_{total} is the total wavefront aberration of coaxial TMA telescope, (x, y) is the coordinates of the field point, $W_H(x, y)$ is the intrinsic field-dependent wavefront aberration under the nominal design state, $W_{PM}(x, y, a5, a6, a7, a8)$ is the contribution of the figure errors of PM to the system aberration, here, the Zernike polynomials are used in wavefront analysis, $a5, a6, a7$ and $a8$ are the coefficients of the 5th to 8th Zernike items respectively, representing the coma and astigmatism. $D_{SMx}, D_{SMy}, D_{SMz}, T_{SMx}, T_{SMy}$ and $D_{TMx}, D_{TMy}, D_{TMz}, T_{TMx}, T_{TMy}$ are five kinds of misalignments of SM and TM respectively, denoting the translation along X, Y, Z and the rotation about X and Y. Here, the rotation about Z is ignored because an coaxial TMA system is considered. $W_{SM}(x, y, D_{SMx}, D_{SMy}, D_{SMz}, T_{SMx}, T_{SMy})$ and $W_{TM}(x, y, D_{TMx}, D_{TMy}, D_{TMz}, T_{TMx}, T_{TMy})$ are respectively the contributions of the misalignments of SM and TM to the system aberrations, including coma, astigmatism and defocus.

As mentioned above, the goal of our optimal compensation strategy is to make W_{total} equal to $W_H(x, y)$ by adding the adjustments of SM described as $\Delta D_{SMx}, \Delta D_{SMy}, \Delta D_{SMz}, \Delta T_{SMx}$ and ΔT_{SMy} to the initial position of SM, as shown in

$$\begin{aligned} &W_{PM}(x,y,a5,a6,a7,a8) \\ &+ W_{SM}(x,y,D_{SMx}+\Delta D_{SMx},D_{SMy}+\Delta D_{SMy}, \\ &D_{SMz}+\Delta D_{SMz},T_{SMx}+\Delta T_{SMx},T_{SMy}+\Delta T_{SMy}) \\ &+ W_{TM}(x,y,D_{TMx},D_{TMy},D_{TMz},T_{TMx},T_{TMy}) \\ &= 0. \end{aligned} \tag{2}$$

From Eq. (2), we can see that how to obtain the solutions of $\Delta D_{SMx}, \Delta D_{SMy}, \Delta D_{SMz}, \Delta T_{SMx}$ and ΔT_{SMy} is the core of the proposed method.

2.2. The nonlinear relationship between the defocus PSF and misalignments of SM

In our method, according to the above optimal compensation strategy, we focus on how to solve $\Delta D_{SMx}, \Delta D_{SMy}, \Delta D_{SMz}, \Delta T_{SMx}$ and ΔT_{SMy} to compensate for the perturbed TMA telescope by using the defocus PSF at the field point of interest. For that purpose, we first built the nonlinear relationship between the defocus PSF and the misalignments of SM, namely $D_{SMx}, D_{SMy}, D_{SMz}, T_{SMx}$ and T_{SMy}. Based on the scalar diffraction theory, a point source f is captured as a single intensity image g after passing through a perturbed TMA telescope with aberrated wavefront φ, which is defined as the PSF. The operation process is written as follows:

$$g = PSF \otimes f, \tag{3}$$

$$PSF = |\mathcal{F}\{W\}|^2, \tag{4}$$

$$W = Ae^{i\varphi}, \tag{5}$$

where $\otimes$ is an operator of the convolution, W is the generalized pupil function, $\mathcal{F}\{\bullet\}$ denotes the operator of two-dimensional Fourier transform, A is the transmittance function of pupil, φ is the system wavefront.

The defocus PSF can be obtained by the same way while the defocus phase $\Delta\Phi$ is added to the wavefront φ, which is expressed as

$$PSF_{defocus} = \left|\mathcal{F}\left\{Ae^{i(\varphi+\Delta\Phi)}\right\}\right|^2, \tag{6}$$

where $PSF_{defocus}$ is the defocus PSF.

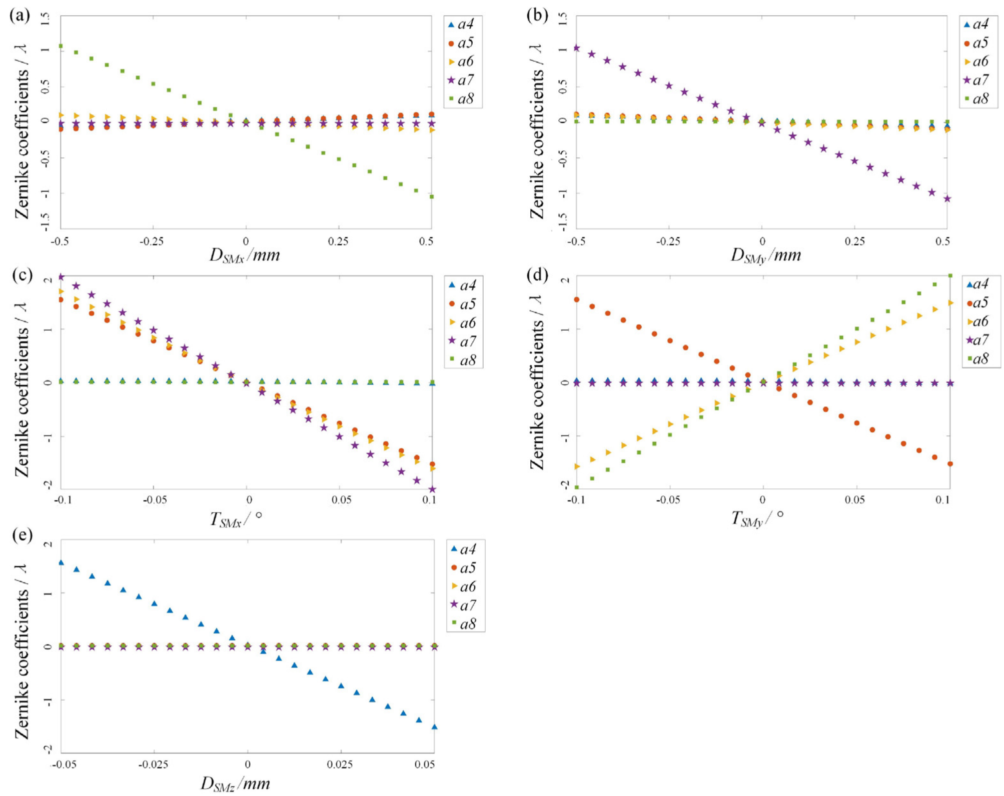

Fig. 1. The variation of Zernike coefficients caused by the misalignments of SM. $a4 \sim a8$ respectively represents the coefficients of the 4th to 8th Zernike items. (a) The change of Zernike coefficients with varied D_{SMx}. (b) The change of Zernike coefficients with varied D_{SMy}. (c) The change of Zernike coefficients with varied T_{SMx}. (d) The change of Zernike coefficients with varied T_{SMy}. (e) The change of Zernike coefficients with varied D_{SMz}.

From Eq. (4) to Eq. (6), we can see that there is a nonlinear relationship between $PSF_{defocus}$ and φ. Theoretically, $D_{SMx}, D_{SMy}, D_{SMz}$, T_{SMx} and T_{SMy} will cause the variation of φ. Here, the variation of φ can be described as Zernike items with coefficients, which is expressed as

$$\Delta\varphi = \sum_{i=1}^{n} (a_i{}' - a_i) Z_i, \tag{7}$$

where $\Delta\varphi$ is the variations of φ, a_i is the ith Zernike coefficient under the nominal design state, and $a_i{}'$ is the ith Zernike coefficient after introducing $D_{SMx}, D_{SMy}, D_{SMz}, T_{SMx}$ and T_{SMy} into the system.

In our simulation, $D_{SMx}, D_{SMy}, D_{SMz}, T_{SMx}$ and T_{SMy} are introduced into the coaxial TMA telescope (taking the preliminary SNAP telescope described in Section 3.1 as the example). D_{SMx}, D_{SMy} are varied over the range of [−0.5 mm, 0.5 mm]. T_{SMx}, T_{SMy} are varied over the range of [−0.1°, 0.1°]. D_{SMz} is varied over the range of [−0.05 mm, 0.05 mm]. As shown in Fig. 1, the relationship between $\Delta\varphi$ and the misalignments of SM is quantitatively analyzed.

It is found that the influences of the misalignments of SM on the high-order aberrations are really small and only the coefficients of the 4th to 8th Zernike items, which represent defocus, coma and astigmatism, are affected by $D_{SMx}, D_{SMy}, D_{SMz}, T_{SMx}$ and T_{SMy}. In general, there is an approximate linear relationship between $\Delta\varphi$ and the misalignments of SM.

Note that STM which is based on the approximate linear relationship between $\Delta\varphi$ and the misalignments of SM can be utilized to obtain the misalignments of SM by employing a dedicated wavefront sensor or PR method. In this paper, we focus on how to obtain the misalignments of SM by using the defocus PSF at the field point of interest, which requires neither a dedicated wavefront sensor nor PR method.

According to Eq. (6), there is a nonlinear relationship between the defocus PSF and $\Delta\varphi$. Furtherly, due to the linear relationship between $\Delta\varphi$ and the misalignments of SM, CNN can be used to establish the mapping between the defocus PSF of the field point of interest and the misalignments of SM so that $D_{SMx}, D_{SMy}, D_{SMz}, T_{SMx}$ and T_{SMy} can be solved according to the defocus PSF at the field point of interest.

2.3. The scheme of aberration compensation by CNN

In order to obtain the adjustments of SM, namely ΔD_{SMx}, ΔD_{SMy}, ΔD_{SMz}, ΔT_{SMx} and ΔT_{SMy}, we first suppose that there exists the misalignments of SM described as D'_{SMx}, D'_{SMy}, D'_{SMz}, T'_{SMx} and T'_{SMy}, the system aberrations induced by them are equivalent to the aberrations of perturbed TMA telescope with low-order figure errors of PM (5th to 8th Zernike items), misalignments of SM ($D_{SMx}, D_{SMy}, D_{SMz}, T_{SMx}, T_{SMy}$) and misalignments of TM ($D_{TMx}, D_{TMy}, D_{TMz}, T_{TMx}, T_{TMy}$), which is expressed as

$$\begin{aligned} &W_{PM}(x, y, a5, a6, a7, a8) \\ &+ W_{SM}(x, y, D_{SMx}, D_{SMy}, D_{SMz}, T_{SMx}, T_{SMy}) \\ &+ W_{TM}(x, y, D_{TMx}, D_{TMy}, D_{TMz}, T_{TMx}, T_{TMy}) \\ &= W_{SM}(x, y, D'_{SMx}, D'_{SMy}, D'_{SMz}, T'_{SMx}, T'_{SMy}). \end{aligned} \tag{8}$$

Then, introducing the additive inverse of D'_{SMx}, D'_{SMy}, D'_{SMz}, T'_{SMx} and T'_{SMy} into the perturbed system, we can get

$$\begin{aligned} &W_{total}(x, y) \\ &= W_H(x, y) + W_{PM}(x, y, a5, a6, a7, a8) \\ &+ W_{SM}(x, y, D_{SMx} - D'_{SMx}, D_{SMy} - D'_{SMy}, \\ &D_{SMz} - D'_{SMz}, T_{TMx} - T'_{TMx}, T_{TMy} - T'_{TMy}) \\ &+ W_{TM}(x, y, D_{TMx}, D_{TMy}, D_{TMz}, T_{TMx}, T_{TMy}). \end{aligned} \tag{9}$$

According to the approximate linear relationship between wavefront aberrations and the misalignments of SM, we can get

$$
\begin{aligned}
&W_{SM}(x,y,D_{SMx}-D'_{SMx},D_{SMy}-D'_{SMy},D_{SMz}-\\
&D'_{SMz},T_{TMx}-T'_{TMx},T_{TMy}-T'_{TMy})\\
&=W_{SM}(x,y,D_{SMx},D_{SMy},D_{SMz},T_{TMx},T_{TMy})\\
&-W_{SM}(x,y,D'_{SMx},D'_{SMy},D'_{SMz},T'_{TMx},T'_{TMy}).
\end{aligned}
\tag{10}
$$

So equation (9) is rewritten as

$$
\begin{aligned}
&W_{total}(x,y)\\
&=W_H(x,y)+W_{PM}(x,y,a5,a6,a7,a8)\\
&+W_{SM}(x,y,D_{SMx},D_{SMy},D_{SMz},T_{TMx},T_{TMy})\\
&-W_{SM}(x,y,D'_{SMx},D'_{SMy},D'_{SMz},T'_{TMx},T'_{TMy})\\
&+W_{TM}(x,y,D_{TMx},D_{TMy},D_{TMz},T_{TMx},T_{TMy}).
\end{aligned}
\tag{11}
$$

Substituting Eq. (8) into Eq. (11), we can see that the system aberrations at the field point of interest can be approximately $W_H(x,y)$, as shown in

$$
\begin{aligned}
&W_{total}(x,y)\\
&=W_H(x,y)+W_{PM}(x,y,a5,a6,a7,a8)\\
&+W_{SM}(x,y,D_{SMx},D_{SMy},D_{SMz},T_{SMx},T_{SMy})\\
&+W_{TM}(x,y,D_{TMx},D_{TMy},D_{TMz},T_{TMx},T_{TMy})\\
&-W_{SM}(x,y,D'_{SMx},D'_{SMy},D'_{SMz},T'_{SMx},T'_{SMy})\\
&=W_H(x,y).
\end{aligned}
\tag{12}
$$

To sum up, the compensation for perturbed system can be implemented by introducing the additive inverse of D'_{SMx}, D'_{SMy}, D'_{SMz}, T'_{SMx} and T'_{SMy} into SM, so the adjustments of SM can be obtained by

$$
\begin{aligned}
&\Delta D_{SMx}=-D'_{SMx},\Delta T_{SMx}=-T'_{SMx},\\
&\Delta D_{SMy}=-D'_{SMy},\Delta T_{SMy}=-T'_{SMy},\\
&\Delta D_{SMz}=-D'_{SMz}.
\end{aligned}
\tag{13}
$$

Apparently, in our method, the implementation of aberration compensation depends on obtaining $D'_{SMx}, D'_{SMy}, D'_{SMz}, T'_{SMx}$ and T'_{SMy}, which will be predicted by CNN.

The scheme of aberration compensation by CNN is shown in Fig. 2. Firstly, for a given coaxial TMA telescope, the nonlinear relationship between the defocus PSF at the field point of interest and the misalignments of SM is established by CNN with the defocus PSF at the field point of interest as the inputs and five kinds of misalignments (the translation along X, Y, Z and the rotation about X and Y) of SM as the outputs. Then, the defocus PSF induced by the perturbed coaxial TMA telescope with misaligned SM and TM and deformed PM is input into the well-trained CNN (named Comp-Net) to predict $D'_{SMx}, D'_{SMy}, D'_{SMz}, T'_{SMx}$ and T'_{SMy}. Finally, $\Delta D_{SMx}, \Delta D_{SMy}, \Delta D_{SMz}$, ΔT_{SMx} and ΔT_{SMy} can be obtained at the field point of interest.

In our method, two alignment schemes either using single-field or multi-field defocus PSFs are proposed to obtain the adjustments of SM. For the single-field alignment, only the defocus PSF at the field point of interest is used to predict the adjustments of SM because the wavefront aberrations of the single field point of interest other than the multiple field points need to be corrected. For the multi-field alignment, considering the imaging requirement for the multiple field points, a field-balanced strategy using multi-field defocus PSFs is proposed. Firstly, according to the intrinsic design of a given coaxial TMA telescope, the number of field points and the position of each field point are determined. Then using the same method as the single-field alignment, the defocus PSF of each field point is input into the Comp-Net respectively to obtain the adjustments of SM associated with each field point, and then, based on the field-balanced strategy, a weight factor associated with the mean square radius of the PSF of each field point is presented, which is expressed as

$$
\begin{cases}
c_i=\dfrac{\iint_{\sigma(x_i,y_i)}\sqrt{(u-u')^2+(v-v')^2}\cdot I(u,v)dudv}{\iint_{\sigma(x_i,y_i)}I(u,v)dudv}\\
w_i=\dfrac{c_i}{\sum_{i=1}^{n}c_i}
\end{cases}
\tag{14}
$$

where c_i is the mean square radius of the PSF of the ith field point, w_i is the weight factor of the ith field point, n is the number of field points, (u,v) is the coordinates of each pixel of the PSF, (u',v') is the centroid coordinates of the PSF, $I(u,v)$ is the light intensity at (u,v), and $\sigma(x_i,y_i)$ is the pixel area of the ith field point [26]. Finally, multiplying the adjustments of SM associated with each field point and the corresponding weight factor based on the field point, the adjustments of SM can be obtained in the case of multi-field alignment, as shown in

$$
\begin{aligned}
&\Delta D_{SMx},\Delta D_{SMy},\Delta D_{SMz},\Delta T_{SMx},\Delta T_{SMy}\\
&=\sum_{i=1}^{n}\{[\Delta D_{SMx}(x_i,y_i),\Delta D_{SMy}(x_i,y_i),\Delta D_{SMz}(x_i,y_i),\\
&\Delta T_{SMx}(x_i,y_i),\Delta T_{SMy}(x_i,y_i)]\cdot w_i\},
\end{aligned}
\tag{15}
$$

where ΔD_{SMx}, ΔD_{SMy}, ΔD_{SMz}, ΔT_{SMx} and ΔT_{SMy} are the adjustments of SM of the multi-field alignment, $\Delta D_{SMx}(x_i,y_i)$, $\Delta D_{SMy}(x_i,y_i)$, $\Delta D_{SMz}(x_i,y_i)$, $\Delta T_{SMx}(x_i,y_i)$ and $\Delta T_{SMy}(x_i,y_i)$ are the adjustments of SM associated with the ith field point.

2.4. Architecture of network

In our study, the Comp-Net shown in Fig. 3 is constructed to map the relationship between the defocus PSF and the misalignments of SM, and trained for the in-orbit aberration compensation. The Comp-Net consists of 9 layers, including 6 convolution layers and 3 fully-connected layers. The network uses 2×2 convolution kernel instead of common 2×2 pool kernel, which can better complete the deep abstract spatial feature extraction. Each convolutional operator is followed by rectified linear unit (Relu) to increase the nonlinear fitting ability. The random dropout layer is used to increase the generalization of the neural network. Through the last fully-connected layer, the image features are mapped to the misalignments of SM. The optimal structure is determined by multiple adjustments according to the changes of loss value in training [27,28].

3. Simulation

In this section, we carry out the simulations of optimal compensation for perturbed coaxial TMA telescope with misaligned SM, TM and deformed PM to verify the effectiveness of our method. The preliminary SNAP telescope is taken as the example to implement the scheme of aberration compensation by CNN shown in Fig. 2, and the corresponding results are obtained. The details are as follows.

3.1. The preliminary SNAP telescope

The preliminary SNAP telescope is a typical coaxial TMA system, which uses a two-meter class optical system with the F number of 10 and the effective focal length of −20,000 mm to deliver diffraction limited images spanned a one degree field in the visible and near infrared wavelength regime. The system structure is shown in Fig. 4 and the structural parameters are listed in Table 1.

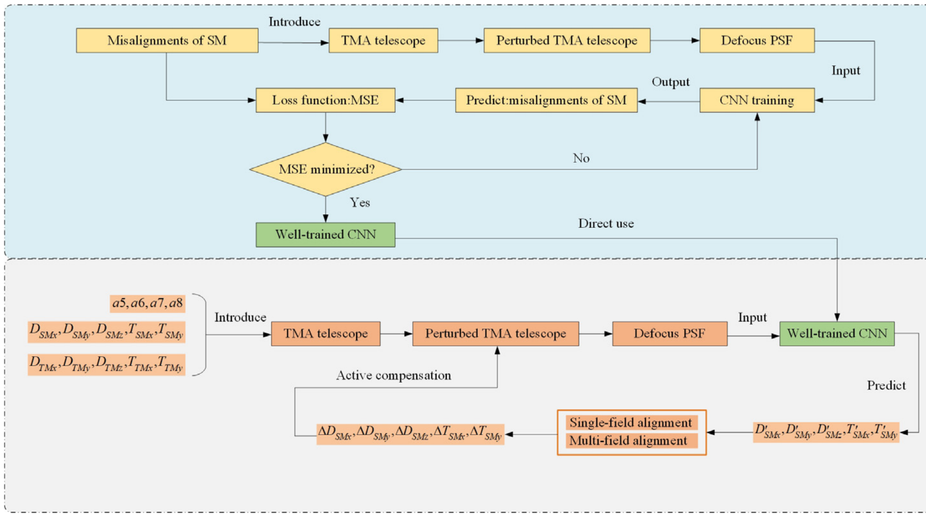

Fig. 2. The schematic diagram of the aberration compensation by CNN.

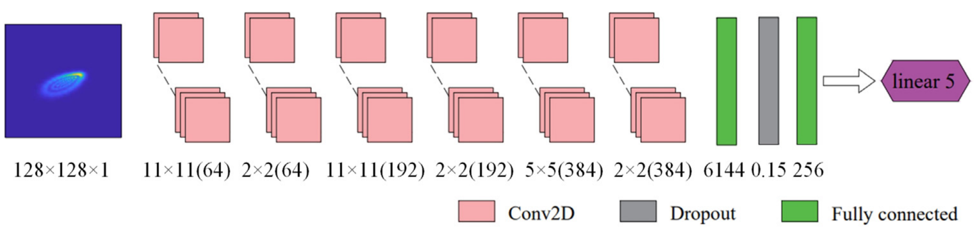

Fig. 3. The architecture of the Comp-Net for predicting the misalignments of SM.

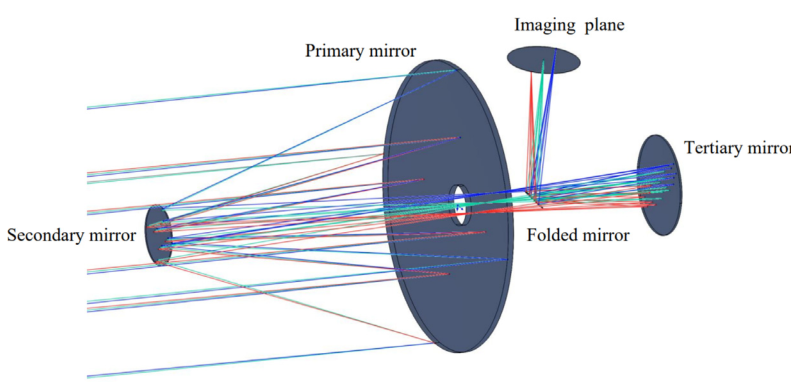

Fig. 4. The structure of preliminary SNAP telescope.

Table 1
Optical prescription of preliminary SNAP telescope.

Surface	Conic coefficient	Radius/mm	Thickness/mm
PM	−0.9745	−5476.9498	−2240.6678
SM	−2.0240	−1249.3071	3800.0000
TM	−0.5490	−1610.9095	−991.4634

Table 2
Dynamic range of the misalignments of SM in training sets.

D_{SMx}/mm	D_{SMy}/mm	D_{SMz}/mm	T_{SMx}/ °	T_{SMy}/ °
± 0.0800	± 0.0800	± 0.0050	± 0.0300	± 0.0300

3.2. Data generation

Obviously, it is high-cost and time-consuming that the actual experiments are operated to add a large number of misalignments into SM to obtain the defocus PSFs for training. In this paper, we establish the optical model of preliminary SNAP telescope for CNN training and the parameters of optical model including wavelength, beam diameter, aperture shape, focal length, field of view, etc., are completely the same as the actual system (described in Section 3.1). Moreover, considering the perturbed characteristics of actual preliminary SNAP telescope, the misalignments of SM vary randomly within the ranges shown in Table 2.

For training the network, 10,000 simulation data are randomly generated, of which 90% are used for the training sets and the others constitute the validation sets. Each set of data takes the defocus PSFs induced by the misalignments of SM as the input and the misalignments of SM as the output. Fig. 5 shows four samples of defocus PSFs induced by different misalignments of SM.

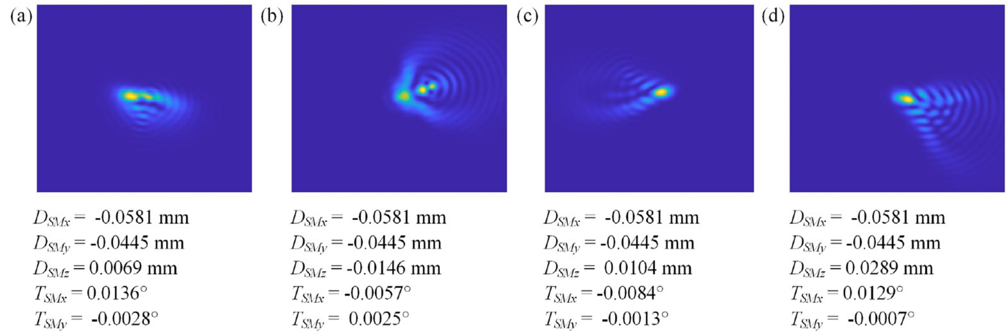

Fig. 5. Four samples of defocus PSFs induced by different misalignments of SM.

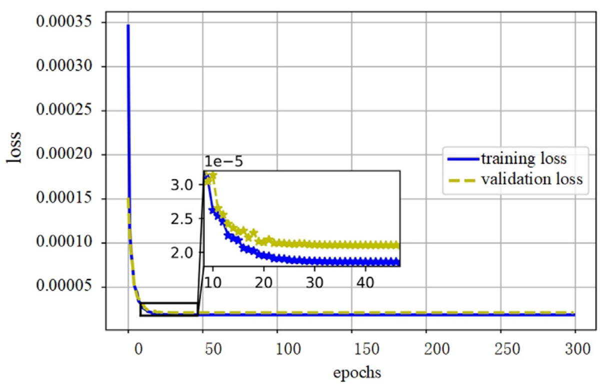

Fig. 6. The evolution of the loss of the Comp-Net.

3.3. Training details and results

The optimizer of the Comp-Net is a dynamically adjusted adaptive moment estimation with an initial learning rate of 1×10^{-4}. The learning rate is a hyper-parameter used to control the rate at which an algorithm updates the parameter estimates or learns the parameter values. The batch size is 128 and the number of epochs is 300. The mean square error (MSE) is chosen as the loss function to quantify the differences between the ground-truth and predicted value of the network, as shown in

$$MSE = \frac{1}{N}\sum_{i=1}^{N}(y_i - {y_i}')^2, \tag{16}$$

where y_i and ${y_i}'$ are the ground-truth and predicted value of the ith data respectively, N is the numbers of data in training sets and validation sets.

The parameters of the Comp-Net are updated iteratively using back-propagated gradients based on the loss value until the predictions of the network are as close as possible to the ground-truth. The entire training process is implemented using the accelerated computation with an NVIDIA GeForce RTX3090.

(−0.5°, 0.5°) is taken as the field point of interest for training. Data generation and CNN training are carried out.

The curve of the loss during CNN training is shown in Fig. 6. It can be seen that the training loss and the validation loss have decreased steadily, which indicates that the Comp-Net has good abilities to predict the misalignments of SM.

For validating the Comp-Net, the defocus PSFs of the validation sets are input into the Comp-Net to directly obtain the misalignments of SM. And the average value of the root mean square error (RMSE) of the misalignments of SM is used to evaluate the accuracy of the Comp-Net and characterize the degree to which the predicted value deviates from the ground-truth, as shown in

$$RMSE = (\frac{\sum_{i=1}^{N}(y_i - {y_i}')^2}{N})^{1/2}, \tag{17}$$

where y_i and ${y_i}'$ are the ground-truth and predicted value of the ith data respectively, N represents the numbers of data.

The RMSE of the misalignments of SM are shown in Table 3. It can be seen that the RMSE of the misalignments of SM are relatively small, indicating that the Comp-Net can accurately predict the misalignments of SM from the defocus PSF. Next, the well-trained Comp can be used to obtain the adjustments of SM to implement the optimal compensation for the perturbed preliminary SNAP telescope.

Table 3
The RMSE of the misalignments of SM.

D_{SMx}/μm	D_{SMy}/μm	D_{SMz}/μm	T_{SMx}/″	T_{SMy}/″
5.6000	5.2000	0.5000	2.1600	2.5200

Table 4
Dynamic range of figure errors of PM.

Zernike coefficient	$a5$	$a6$	$a7$	$a8$
RMS range/λ	$\pm0.1\lambda$	$\pm0.1\lambda$	$\pm0.1\lambda$	$\pm0.1\lambda$

Table 5
Dynamic range of misalignments of SM.

D_{SMx} /mm	D_{SMy} /mm	D_{SMz} /mm	T_{SMx}/ °	T_{SMy}/ °
± 0.0400	± 0.0400	± 0.0050	± 0.0100	± 0.0100

Table 6
Dynamic range of misalignments of TM.

D_{TMx} /mm	D_{TMy} /mm	D_{TMz} /mm	T_{TMx}/ °	T_{TMy}/ °
± 0.0400	± 0.0400	± 0.0050	± 0.0100	± 0.0100

3.4. The optimal compensation with SM

We utilize the scheme shown in Fig. 2 to implement the optimal compensation for perturbed preliminary SNAP telescope with misaligned SM, TM and deformed PM.

Firstly, the optical model of perturbed preliminary SNAP telescope is built. According to the practical application, 100 data with different low-order figure errors of PM, and misalignments of SM and TM within the ranges shown in Tables 4 to 6 are randomly generated and input into the preliminary SNAP telescope.

Then, based on the scalar diffraction theory, the corresponding defocus PSFs of the field point of interest of perturbed preliminary SNAP telescope are obtained, which can be input into the Comp-Net to directly predict the adjustments of SM associated with the field point

Table 7
RMS values of the wavefront aberration before and after the aberration compensation at the field point (−0.5°, 0.5°).

	Average RMS/λ	Std RMS/λ
Before the aberration compensation	0.5893	0.2466
After the aberration compensation	0.0845	0.0243

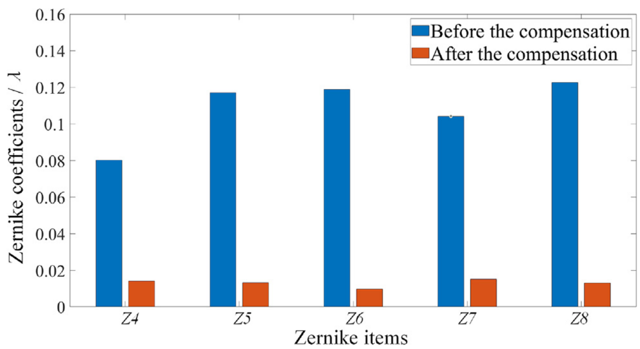

Fig. 7. Comparisons of Zernike coefficients before and after the compensation at the field point (−0.5°, 0.5°).

of interest. In our study, two alignment schemes either using single-field or multi-field defocus PSFs are carried out to obtain the final adjustments of SM by multiplying the outputs of the Comp-Net and the weight factor based on the field point.

Finally, the adjustments of SM are input into the perturbed preliminary SNAP telescope and the aberration compensation is completed by adjusting SM.

In this paper, the Root Mean Square (RMS) of residual wavefront after the compensation is used to evaluate the accuracy of aberration compensation, as shown in

$$RMS = \sqrt{\frac{\sum_{i=1,j=1}^{m,n}\left[W(i,j)-\overline{W}\right]^2}{N}}, \tag{18}$$

where, $W(i,j)$ is the wavefront aberration at the point (i,j), $\overline{W}$ is the average value of the wavefront aberration of all sampling points, and N is the total number of sampling points.

4. Results and analysis

4.1. The compensation results of the single-field alignment scheme

The RMS values of wavefront aberration at the field point (−0.5°, 0.5°) before and after the compensation are shown in Table 7.

From Table 7, after the aberration compensation, the average RMS of residual wavefront aberrations can be reduced from about 0.59 λ to 0.08 λ, and the standard deviation (Std) RMS of residual wavefront aberrations can be reduced from about 0.25 λ to 0.02 λ, which show that the perturbed system almost has been recovered to the nominal design. The changes of residual wavefront represented by the 4th to 8th Zernike coefficients before and after the compensation are given in Fig. 7. It can be seen that defocus, coma, astigmatism at the field point of interest are greatly corrected by utilizing the proposed method.

Fig. 8 shows the comparisons of the focus PSFs at the field point (−0.5°, 0.5°) before and after the compensation. Here we present four examples which have different initial perturbed states. The first row is the initial perturbed focus PSFs before the compensation, and the second row is the corresponding focus PSFs after the compensation. It can be seen that after the compensation, the initial irregular dispersion blurring state of the spot is improved, the energy of the spot is concentrated, and the image quality is significantly improved. It is verified again that the proposed method can realize the in-orbit aberration compensation at the field point of interest.

4.2. The compensation results of the multi-field alignment scheme

In our study, four field points namely (−0.5°, 0.5°), (−0.5°, −0.5°), (0.5°, −0.5°) and (0.5°, 0.5°) are selected to perform the multi-field alignment. The dynamic ranges of the low-order figure errors of PM and the misalignments of SM and TM are the same as those of the single-field alignment scheme. The RMS values of wavefront aberration at each field point before and after the compensation are shown in Table 8.

Obviously, from Table 8, the aberrations of each field point are compensated for based on the field-balanced strategy. In general, the RMS values of wavefront aberrations of multi-field can be reduced from about 0.59 λ to 0.12 λ.

In addition, for the selected field points, the changes of residual wavefront represented by the Zernike coefficients before and after the compensation are shown specifically in Fig. 9. From Fig. 9, the coma can be well eliminated and the astigmatism can be balanced by using the multi-field alignment scheme.

Fig. 10 shows the comparisons of the focus PSFs at five field points before and after the compensation. The first row is the initial perturbed focus PSFs before the compensation, and the second row is the corresponding focus PSFs after the compensation. Similarly, it can be seen that after the compensation, the image quality is improved. It is also verified that the proposed method can realize the in-orbit aberration compensation based on the field-balanced strategy.

In summary, the two proposed alignment schemes either using single-field or multi-field defocus PSFs can be used for aberration compensation with high accuracy. Compared with the existing compensation methods, the proposed method requires neither a dedicated wavefront sensor nor driving active correction components repeatedly nor a lot of iterations to optimize a metric function, which is suitable for in-orbit active fast compensation for perturbed coaxial TMA telescope.

4.3. The influences of noise and high-order figure errors of PM on compensation

As mentioned above, it is impractical and high-cost to accomplish the network training by adding a large number of misalignments into SM through actual experiments. In this section, we focus on the influences of the high-order figure errors of PM and image noise on the accuracy of aberration compensation so as to make sure our simulations are consistent with the actual situations.

The RMS value of residual wavefront aberration is still used to evaluate the accuracy of aberration compensation, and the quantitative results of the influences of various factors on the accuracy of aberration compensation are obtained, which are described as follows.

4.3.1. Noise

Apparently, the image noise will affect the light intensity distribution of the defocus PSF. Signal-to-Noise Ratio (SNR) measures the strength of the signal relative to the background noise, which is defined as

$$SNR(dB) = 20\log_{10}\frac{\|I(u,v)\|}{\|noise\|} \tag{19}$$

The Gaussian noises with SNR of 30,40 and 50 are added to the test data respectively and 100 new test data are generated in total. Fig. 11 shows that defocus PSF under Gaussian noises with different SNR. Then the test data are input into the Compe-Net, and the corresponding accuracies of aberration compensation are shown in Table 9.

It can be seen from Table 9 that when the SNR decreases, the RMS of residual wavefront aberration will increase accordingly. When SNR is higher than 30 dB, the compensation accuracy can be controlled within 0.085 λ RMS, which indicates that the Compe-Net suppresses the influence of some noises when image features are being extracted. The proposed method has good robustness to noise.

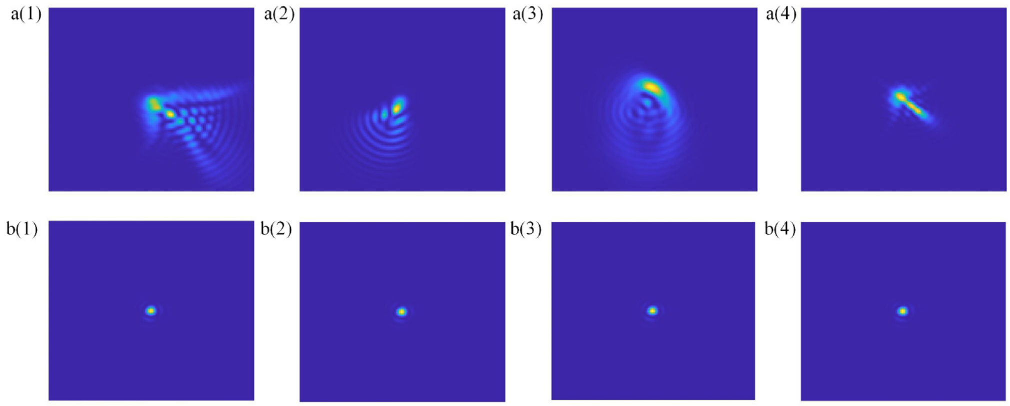

Fig. 8. Comparisons of focus PSFs before and after the compensation. (a(1) ~ a(4)) Before the compensation. (b(1) ~ b(4)) After the compensation.

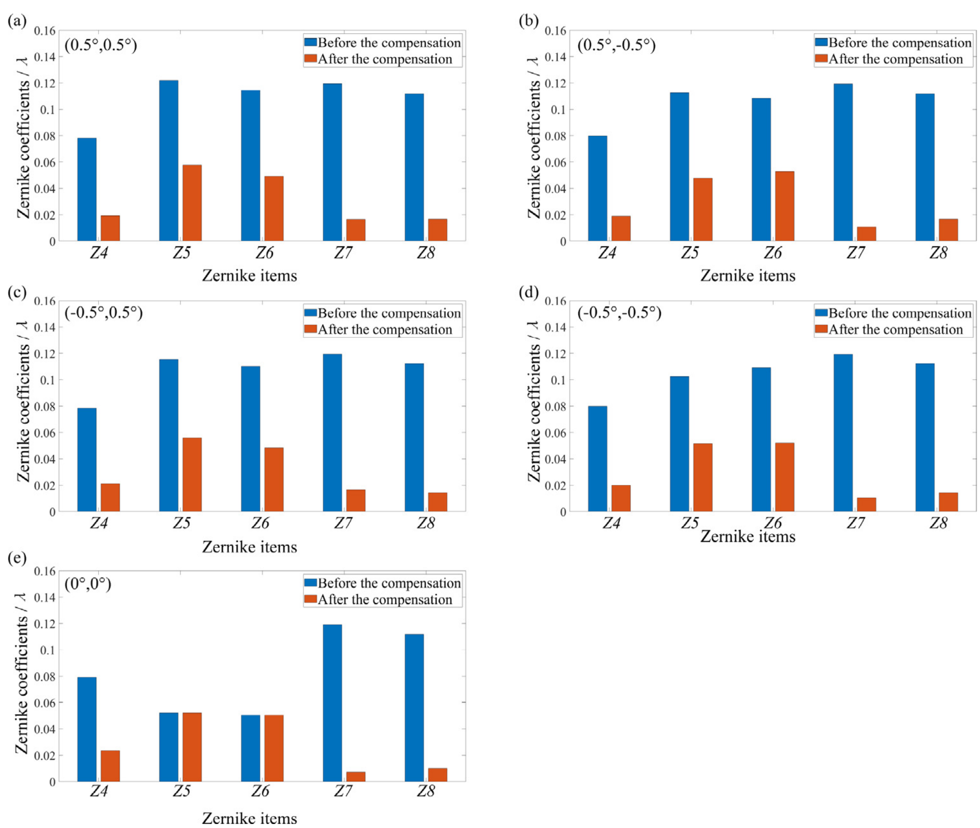

Fig. 9. Comparisons of Zernike coefficients before and after the aberration compensation (five field points).

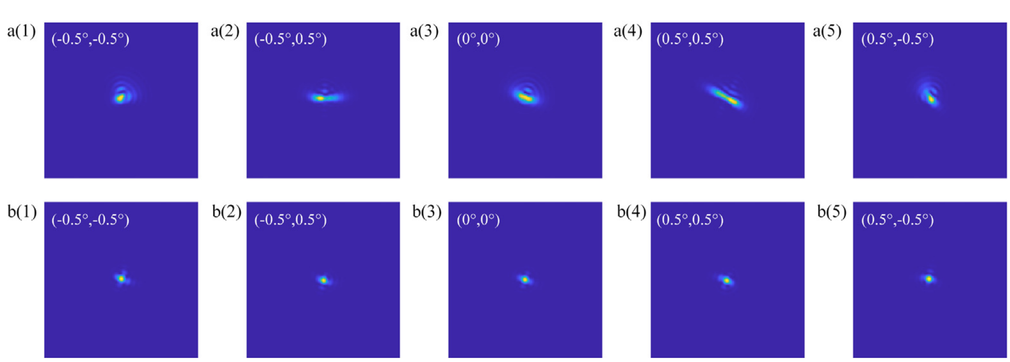

Fig. 10. Comparisons of focus PSFs before and after the aberration compensation (five field points).

Table 8
RMS values of wavefront aberration at five field points before and after the aberration compensation.

Field point	Before the aberration compensation		After the aberration compensation	
	Average RMS/λ	Std RMS/λ	Average RMS/λ	Std RMS/λ
(0°, 0°)	0.5644	0.2452	0.0921	0.0299
(−0.5°, 0.5°)	0.5893	0.2466	0.1174	0.0273
(−0.5°, −0.5°)	0.5889	0.2495	0.1182	0.0303
(0.5°, 0.5°)	0.5971	0.2490	0.1155	0.0318
(0.5°, −0.5°)	0.5871	0.2516	0.1170	0.0291

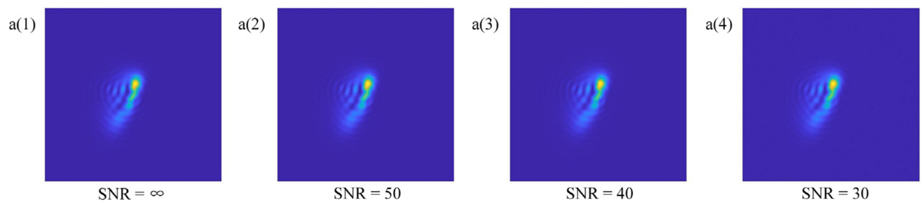

Fig. 11. Defocus PSF under Gaussian noises with different SNR.

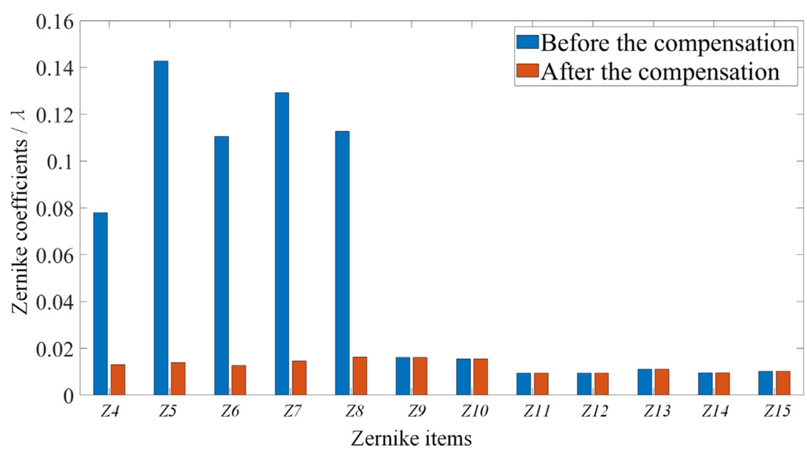

Fig. 12. Comparisons of Zernike coefficients before and after the aberration compensation in case of high-order figure errors of PM existing.

Table 9
The RMS of residual wavefront aberration under Gaussian noises with different SNR.

SNR/dB	∞	50	40	30
Average RMS/λ	0.0844	0.0844	0.0845	0.0847

Table 10
The high-order figure errors of PM.

Zernike coefficient	$a9$	$a10$	$a11$	$a12$	$a13$	$a14$	$a15$
RMS range/λ	± 0.02	± 0.02	± 0.02	± 0.02	± 0.02	± 0.02	± 0.02

4.3.2. *High-order figure errors of PM*

In practical application, the high-order figure errors of PM exist inevitably. In the case of single-field alignment scheme, we study the influence of the high-order figure errors of PM (represented by the 9th to 15th Zernike items) on the accuracy of compensation. The high-order figure errors of PM are added to the perturbed preliminary SNAP telescope to generate the corresponding defocus PSFs, then, the defocus PSFs are input into the Compe-Net for testing. In our study, the 9th to 15th Zernike coefficients vary randomly within the ranges shown in Table 10, and the dynamic ranges of the low-order figure errors of PM, and the misalignments of SM and TM are the same as those in Section 3.4.

The accuracies of aberration compensation are shown in Table 11 and the changes of residual wavefront represented by Zernike coefficients before and after the compensation are shown in Fig. 12.

Table 11
RMS values of wavefront before and after the aberration compensation in case of high-order figure errors of PM existing.

	Average RMS/λ	Std RMS/λ
Before the aberration compensation	0.5993	0.2462
After the aberration compensation	0.1133	0.0370

It can be seen that the proposed method can still significantly reduce the RMS of residual wavefront in case of high-order figure errors of PM existing, but compared with the results shown in Table 7, the compensation effect declines. The main reason is that high-order figure errors of PM cannot be compensated for by only adjusting SM. As shown in Fig. 12, the 9th to 15th Zernike coefficients have not changed after the compensation. Besides, comparing Fig. 12 with Fig. 7, we find that the proposed method can still significantly reduces the RMS of the residual wavefront although the compensation capacity on the 4th to 8th Zernike items is dropped slightly with the introduction of high-order figure errors of PM, which verifies that the Comp-Net has good generalization abilities.

4.4. *The comparisons with STM*

STM is a common method for calculating the adjustments of SM, which has been widely used for active compensation for perturbed coaxial TMA telescope. The compensation accuracy of STM is limited to the wavefront sensing error because it requires employing a wavefront sensor (such as SH) or PR method to sense the wavefront aberration.

For STM, due to the commercial SHs having the sensing accuracy of $\lambda/100$ RMS and high sensing speed, the compensation accuracy and efficiency become relatively high, however, the use of a dedicated wavefront sensor will increase the complexity and cost of the system. PR method performs massive computations, which is time-consuming.

The proposed method only needs defocus PSFs to calculate the adjustments of SM, and no extra hardware devices and expense are needed. When a defocus PSF is input into the Comp-Net, it takes only 0.035 s to obtain the adjustments of SM, which has the outstanding performance in the correction efficiency.

5. Conclusion

In this paper, an active compensation method for perturbed CRST based on defocus PSF and CNN is proposed, and the TMA telescope is used as an example to illustrate our method. Two alignment schemes either using single-field or multi-field defocus PSFs are proposed to obtain the adjustments of SM by multiplying the outputs of well-trained CNN and the weight factor based on the field point. In case of single-field alignment, the RMS of wavefront aberration can be approximately to the nominal design state, and defocus, coma and astigmatism are basically eliminated. For the multi-field alignment, the aberration at each field point can be compensated for by a field-balanced strategy. The simulation proofs show that the proposed method can implement an in-orbit active fast compensation for perturbed CRST with misaligned SM and TM and deformed PM by obtaining the adjustments of SM according to the selected field points and corresponding defocus PSF.

Declaration of competing interest

The authors declare that they have no known competing financial interests or personal relationships that could have appeared to influence the work reported in this paper.

Data availability

Data will be made available on request

References

[1] E. Zackrisson, A. Zitrin, M. Trenti, C.-E. Rydberg, L. Guaita, D. Schaerer, T. Broadhurst, G. Östlin, T. Ström, Detecting gravitationally lensed Population III galaxies with the Hubble Space Telescope and the James Webb Space Telescope, Mon. Not. R. Astron. Soc. 427 (3) (2012) 2212–2223.

[2] A. Vikaeus, E. Zackrisson, D. Schaerer, E. Visbal, E. Fransson, S. Malhotra, J. Rhoads, M. Sahlén, Conditions for detecting lensed Population III galaxies in blind surveys with the James Webb Space Telescope, the Roman Space Telescope, and Euclid, Mon. Not. R. Astron. Soc. 512 (2) (2022) 3030–3044.

[3] P. Zhou, D. Zhang, G. Liu, C. Yan, Development of space active optics for a whiffletree supported mirror, Appl. Opt. 58 (21) (2019) 5740–5747, http://dx.doi.org/10.1364/AO.58.005740.

[4] N. Devaney, F. Kenny, A.V. Goncharov, M. Goy, C. Reinlein, Development of a prototype active optics system for future space telescopes, Appl. Opt. 57 (22) (2018) E101–E106, http://dx.doi.org/10.1364/AO.57.00E101.

[5] P. Martinez, J. Kolb, M. Sarazin, J. Navarrete, Active optics Shack–Hartmann sensor: using spot sizes to measure the seeing at the focal plane of a telescope, Mon. Not. R. Astron. Soc. (ISSN: 0035-8711) 421 (4) (2012) 3019–3026, http://dx.doi.org/10.1111/j.1365-2966.2012.20527.x, arXiv:https://academic.oup.com/mnras/article-pdf/421/4/3019/3801355/mnras0421-3019.pdf.

[6] H. Ma, H. Liu, Y. Qiao, X. Li, W. Zhang, Numerical study of adaptive optics compensation based on convolutional neural networks, Opt. Commun. (ISSN: 0030-4018) 433 (2019) 283–289, http://dx.doi.org/10.1016/j.optcom.2018.10.036.

[7] D.S. Acton, J.S. Knight, Multi-field alignment of the james webb space telescope, Proc. SPIE - Int. Soc. Opt. Eng. (2012).

[8] M. Wen, C. Han, H. Ma, Active compensation for optimal RMS wavefront error in perturbed off-axis optical telescopes using nodal aberration theory, Appl. Opt. 60 (6) (2021) 1790–1800, http://dx.doi.org/10.1364/AO.414596.

[9] X. Zhang, S. Xu, H. Ma, N. Liu, Optical compensation for the perturbed three mirror anastigmatic telescope based on nodal aberration theory, Opt. Express 25 (11) (2017) 12867–12883, http://dx.doi.org/10.1364/OE.25.012867.

[10] E.D. Kim, Y.W. Choi, M.S. Kang, S.C. Choi, Reverse-optimization Alignment Algorithm using Zernike Sensitivity, J. Opt. Soc. Korea (2005).

[11] S. Kim, H.S. Yang, Y.W. Lee, S.W. Kim, Merit function regression method for efficient alignment control of two-mirror optical systems, Opt. Express 15 (8) (2007) 5059–5068.

[12] Z. Gu, C. Yan, Y. Wang, Alignment of a three-mirror anastigmatic telescope using nodal aberration theory, Opt. Express 23 (19) (2015) 25182.

[13] G. Ju, C. Yan, Z. Gu, H. Ma, Computation of astigmatic and trefoil figure errors and misalignments for two-mirror telescopes using nodal-aberration theory, Appl. Opt. (2016).

[14] Z. Li, X. Yuan, X. Cui, Alignment metrology for the Antarctica Kunlun Dark Universe Survey Telescope, Mon. Not. R. Astron. Soc. (ISSN: 0035-8711) 449 (1) (2015) 425–430, http://dx.doi.org/10.1093/mnras/stv268, arXiv:https://academic.oup.com/mnras/article-pdf/449/1/425/4133295/stv268.pdf.

[15] Z. Liu, P. Qi, Y. Xu, H. Ma, G. Ren, Misalignment calculation on off-axis telescope system via fully connected neural network, IEEE Photonics J. PP (99) (2020) 1.

[16] Y. Carmon, E.N. Ribak, Phase retrieval by demodulation of a Hartmann–Shack sensor, Opt. Commun. (ISSN: 0030-4018) 215 (4) (2003) 285–288, http://dx.doi.org/10.1016/S0030-4018(02)02254-X.

[17] C. Li, B. Li, S. Zhang, Phase retrieval using a modified Shack–Hartmann wavefront sensor with defocus, Appl. Opt. 53 (4) (2014) 618–624.

[18] D.S. Acton, J.S. Knight, A. Contos, S. Grimaldi, J. Terry, P. Lightsey, A. Barto, B. League, B. Dean, J.S. Smith, Wavefront sensing and controls for the james webb space telescope, Space Telescopes and Instrumentation 2012: Optical, Infrared, and Millimeter Wave 8442 (2012) 84422H.

[19] S. Zommer, E.N. Ribak, S.G. Lipson, J. Adler, Simulated annealing in ocular adaptive optics, Opt. Lett. 31 (7) (2006) 939–941, http://dx.doi.org/10.1364/OL.31.000939.

[20] D.B. Conkey, A.N. Brown, A.M. Caravaca-Aguirre, R. Piestun, Genetic algorithm optimization for focusing through turbid media in noisy environments, Opt. Express 20 (5) (2012) 4840–4849, http://dx.doi.org/10.1364/OE.20.004840.

[21] M.A. Vorontsov, V.P. Sivokon, Stochastic parallel-gradient-descent technique for high-resolution wave-front phase-distortion correction, J. Opt. Soc. Amer. A 15 (10) (1998) 2745–2758.

[22] H. Ren, B. Dong, Y. Li, Alignment of the active secondary mirror of a space telescope using model-based wavefront sensorless adaptive optics, Appl. Opt. 60 (8) (2021) 2228–2234, http://dx.doi.org/10.1364/AO.415435.

[23] Z. Li, J. Su, X. Zhao, Atmospheric turbulence compensation with sensorless AO in OAM-FSO combining the deep learning-based demodulator, Opt. Commun. (ISSN: 0030-4018) 460 (2020) 125111, http://dx.doi.org/10.1016/j.optcom.2019.125111.

[24] P. Jia, X. Li, Z. Li, W. Wang, D. Cai, Point spread function modelling for wide-field small-aperture telescopes with a denoising autoencoder, Mon. Not. R. Astron. Soc. (ISSN: 0035-8711) 493 (1) (2020) 651–660, http://dx.doi.org/10.1093/mnras/staa319, arXiv:https://academic.oup.com/mnras/article-pdf/493/1/651/32513220/staa319.pdf.

[25] K.P. Thompson, T. Schmid, P.R. Jannick, The misalignment induced aberrations of TMA telescopes, Opt. Express (2008).

[26] R.A. Muller, A. Buffington, Real-time correction of atmospherically degraded telescope images through image sharpening, J. Opt. Soc. Amer. 64 (9) (1974) 1200–1210, http://dx.doi.org/10.1364/JOSA.64.001200.

[27] J. Schmidhuber, Deep learning in neural networks, Neural Netw. (2015).

[28] S. Ioffe, C. Szegedy, Batch normalization: Accelerating deep network training by reducing internal covariate shift, JMLR.Org (2015).